

RESEARCH ARTICLE

10.1002/2016JE005048

Key Points:

- Magnetic anomalies are concentrated near and within the Caloris impact basin and an unnamed older basin associated with Sobkou Planitia
- Anomalies within Caloris imply that Mercury had a core dynamo when this basin formed ca. 3.9 Gyr ago
- Anomalies are weak over high-reflectance volcanic plains and are strong over low-reflectance material

Supporting Information:

- Supporting Information S1

Correspondence to:

L. L. Hood,
lon@lpl.arizona.edu

Citation:

Hood, L. L. (2016), Magnetic anomalies concentrated near and within Mercury's impact basins: Early mapping and interpretation, *J. Geophys. Res. Planets*, 121, 1016–1025, doi:10.1002/2016JE005048.

Received 5 APR 2016

Accepted 21 MAY 2016

Accepted article online 30 MAY 2016

Published online 15 JUN 2016

Magnetic anomalies concentrated near and within Mercury's impact basins: Early mapping and interpretation

L. L. Hood¹
¹Lunar and Planetary Laboratory, University of Arizona, Tucson, Arizona, USA

Abstract Ninety-five low-altitude passes of MErcury Surface, Space ENvironment, GEochemistry, and Ranging magnetometer data from February, March, and April of 2015 have been applied to produce an approximate map of the crustal magnetic field at a constant altitude of 40 km covering latitudes of 35°–75°N and longitudes of 90°–270°E. Anomalies are concentrated near and within the Caloris impact basin. A smaller concentration occurs over and around Sobkou Planitia and an associated older large impact basin. The strongest anomalies are found within Caloris and are distributed in a semicircular arc that is roughly concentric with the basin rim. They imply the existence of a core dynamo at the time when Caloris formed (~3.9 Gyr ago). Anomalies over high-reflectance volcanic plains are relatively weak while anomalies over low-reflectance material that has been reworked by impact processes are relatively strong. The latter characteristics are qualitatively consistent with the ejecta deposit model for anomaly sources.

1. Introduction

The NASA MErcury Surface, Space ENvironment, GEochemistry, and Ranging (MESSENGER) Discovery mission has obtained a very valuable data set for investigating crustal magnetism at Mercury [Johnson *et al.*, 2015]. Low-altitude magnetometer data from August to September of 2014 have previously been applied to construct a preliminary map of the crustal field at 80 km altitude covering latitudes of 50°–80°N and longitudes of 160°–330°E [Hood, 2015; hereafter H15]. It was found that the strongest anomalies within the mapped region were located just north and northeast of the Caloris impact basin. Strong anomalies occurred over smooth plains that are part of a circumferential belt of plains around Caloris [Denevi *et al.*, 2013] and over the Odin Formation (interpreted as primary Caloris basin ejecta [Guest and Greeley, 1983]). It was therefore proposed that many of the Mercurian anomaly sources consist of impact basin ejecta materials.

However, MESSENGER magnetometer data from the last few months of the mission (February–April 2015), during which the periaapsis altitude remained relatively low and external field interference was minimal, are now available in the Planetary Data System. These data allow mapping of crustal fields at lower altitudes over a wider area than was previously possible. Most importantly, the southern boundary of the mapping area can be extended southward from 50°N to 35°N, providing some coverage over Caloris itself. As will be seen, the resulting maps provide further evidence for an association of Mercury's crustal magnetic anomalies with impact basins, show that anomalies are mainly strongest within Caloris itself, and also yield new constraints on the history of the core dynamo.

2. Mapping Methods

As discussed in H15, the eccentricity of MESSENGER's orbit combined with the need for periodic correction burns resulted in a very variable spacecraft altitude during those periods when crustal fields could be measured. An equivalent source dipole (ESD) technique [e.g., von Frese *et al.*, 1981; Purucker *et al.*, 2000; Langlais *et al.*, 2004] is therefore necessary to construct approximate maps at a constant altitude.

Figure 1a plots the surface tracks of 95 orbits of MESSENGER calibrated magnetometer data within the northern midlatitude region that was selected for mapping (90°E to 270°E, 35°N to 75°N). Figure 1b plots the spacecraft altitude in kilometers along these orbit tracks. As indicated in Figure 1b, the selected orbits were from two periods during February–March and April of 2015, which provided continuous coverage at low altitudes within the 90°E to 270°E longitude sector. Specifically, orbit passes from 26 February to 24 March were first selected to cover longitudes from 90°E to about 230°E. Then passes from 16 April to 26 April were used

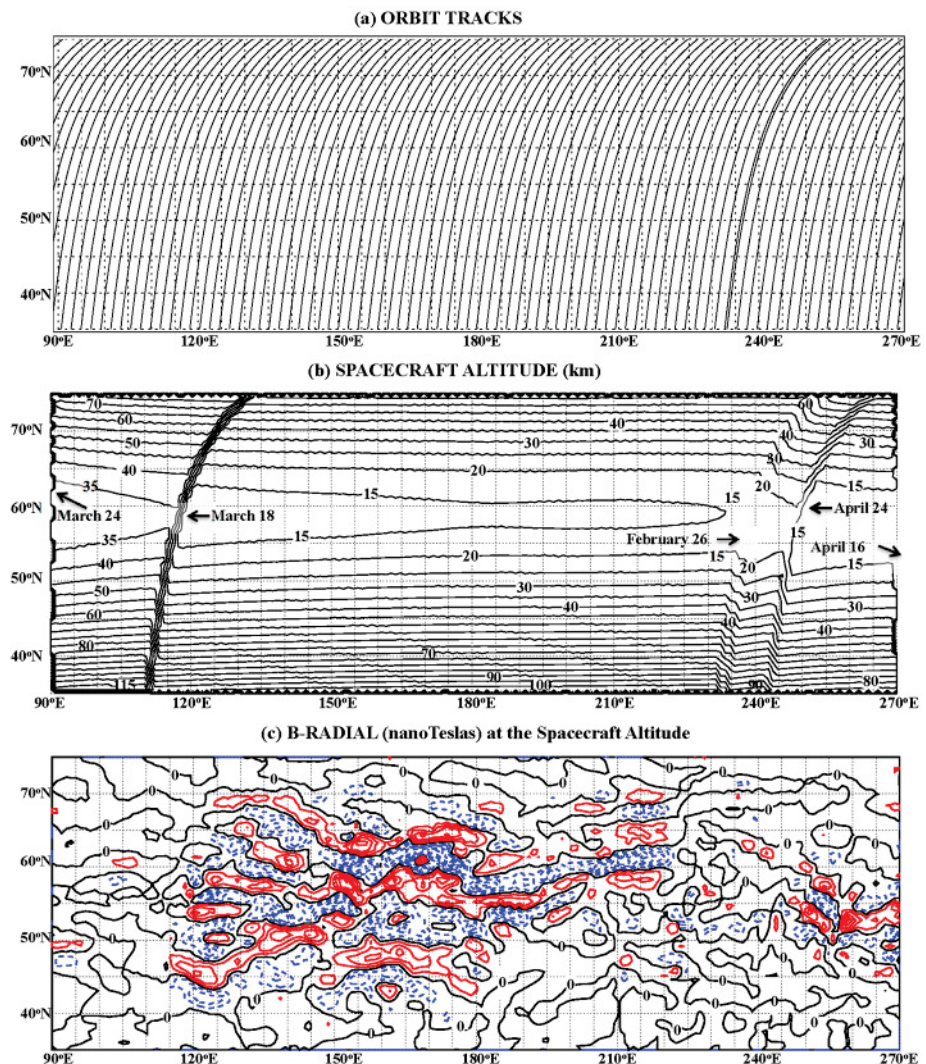


Figure 1. Summary of the selected MESSENGER data from February, March, and April of 2015: (a) orbit tracks; (b) spacecraft altitude; and (c) radial magnetic field intensity at the spacecraft altitude. In Figure 1c, the contour interval is 2 nT and negative dashed contours are blue; positive contours are red.

to complete the coverage from about 230°E to 270°E. Periapsis altitudes ranged from as little as 12 km in mid-March and April to more than 30 km in late March. Sudden changes in altitude occurred on 18 March and 24 April because of orbit correction burns. In addition, a change in altitude occurs between the beginning of the first group of orbit passes on 26 February and the end of the April passes on 26 April. The altitude also increases rapidly with distance from 60°N. Near 35°N, the spacecraft altitude is as large as 105 km at longitudes from about 120°E to 230°E but is less than 90 km eastward of 235°E. At longitudes of 90°E to 110°E, spacecraft altitudes are as high as 115–120 km near 35°N.

Despite the large variation in altitude, it is instructive to first map the radial component of the measured crustal field at the spacecraft altitude (Figure 1c). The radial field component is chosen because it is usually less affected by transient external fields. As described previously in H15, to construct the map a series of steps must be taken including (a) filtering to minimize long-wavelength fields of noncrustal origin; (b) editing the residuals to minimize short-wavelength variations that do not repeat on successive orbit passes; and (c) two-dimensionally filtering the remaining data after sorting into 0.5° latitude by 1° longitude bins.

As illustrated in Figure S1 in the supporting information, filtering was accomplished in two substeps. First, a cubic polynomial was least squares fitted to the raw radial component time series (Figure S1a) for each orbit pass from 32.5°N to 77.5°N. As seen in Figure S1b, this removes much of the internal planetary and

magnetospheric field but a small long-wavelength residual remains. To eliminate the residual, the deviation from 5° latitude running averages was calculated as illustrated in Figure S1c. In effect, wavelengths greater than approximately 5° of latitude (about 215 km) are eliminated by this procedure. Johnson *et al.* [2015] have taken the alternate approach of subtracting a magnetospheric model field from the raw radial field data rather than cubic detrending. However, a long-wavelength residual also remains after subtracting the model field so high-pass filtering must still be applied. Both methods therefore appear to be equally effective, so the simpler cubic detrending approach is used here. Maximum wavelengths of 215 km correspond to source depths of no more than about 100 km, guaranteeing that the final high-pass fields are dominantly of crustal origin.

Next, the filtered radial field data were visually examined to identify short-wavelength magnetic variations that did not repeat on successive orbit passes, due to the presence of external field noise. Any such periods were edited out of the time series. Careful editing (i.e., eliminating even small deviations that do not repeat on adjacent passes) was especially necessary near the southern mapping boundary (35°N) where the spacecraft altitude was increasing rapidly because small spurious variations at high altitudes can be amplified by the ESD technique when continued to a lower altitude.

Finally, the data were sorted into 0.5° latitude by 1.0° longitude bins and were two-dimensionally filtered once using a 5 by 5 bin boxcar filter. This produces a map of the radial field component at the (variable) spacecraft altitude. As shown in Figure 1c, as expected, the strongest fields are mapped where the spacecraft altitude was lowest, especially at longitudes from 120°E to 220°E. Radial anomalies are mapped along the northern rim of the Caloris basin (centered at about 160°E, 30°N), but no significant anomalies are mapped within the basin at the southern boundary because of the high spacecraft altitude. Similarly, no significant anomalies are mapped near the Sobkou basin (centered at about 225°E, 35°N).

In order to adjust the filtered radial field data to a constant altitude, a relatively simple “classical ESD” technique [e.g., Purucker *et al.*, 2000] is adopted in which the sources are assumed to consist of an array of vertically oriented dipoles separated by 1° in latitude and 2° in longitude (3731 dipoles) on a spherical surface at a chosen depth. Although more advanced techniques involving spherical cap harmonic analysis [Thebaud *et al.*, 2006] and regional wavelet analysis [Holschneider *et al.*, 2003] have been developed, the classical method is considered to be sufficient for the present application. Figure S2a indicates schematically the assumed distribution of equivalent source dipoles. To improve computational efficiency, the array was divided into a series of six overlapping 40° longitude sectors as shown in Figure S2b. Also, the number of data points along a given orbit track was reduced by calculating averages in 0.1° latitude segments. The same computational method described in H15 was adopted except that the amplitude of the dipole moment increment after each iteration was variable. Specifically, all dipole moment amplitudes were initially set at $+1.0 \text{ G km}^3$ (10^{12} A m^2) and the amplitude increment after each iteration was initially set to $\pm 0.1 \text{ G km}^3$. After 40 iterations, the increment was reduced by a factor of 2. As illustrated in Figure S2c, convergence to an approximate solution (defined as occurring when the change in RMS deviation after a given iteration decreases to of order 0.001 nT) was found to occur typically after about 100 iterations. As in the analysis of H15, results were not found to be strongly sensitive to the chosen exactly radial orientation of the model dipoles. Repetition of the analysis assuming that all dipoles are tilted by 45° southward from vertical yields nearly identical results (see Figure S1 of H15). Results are somewhat more sensitive to the assumed depth of the dipole array (see Figure S2 of H15). Trial calculations were therefore performed for a series of assumed depths at 5 km intervals. A dipole source depth of about 20 km yields a minimum RMS deviation for this data set and for the assumed dipole spacing. This in no way implies that the actual sources of Mercury’s crustal field lie 20 km beneath the surface. Distributed sources near the surface can produce fields at the spacecraft altitude that are nearly indistinguishable from those of point dipoles buried at 20 km depth.

As in H15, the complete array of 91 by 41 model dipoles was obtained from the overlapping individual sector solutions. The last 5° of the first sector (90°E to 130°E) and the first 5° of the second sector (120°E to 160°E) were discarded to avoid edge effects. This was repeated for the remaining sectors. The three model vector field components and field magnitude were then calculated along the original 95 orbit tracks at a constant altitude of 40 km. Final RMS deviations (misfits) in a given sector ranged from 0.33 to 0.69 nT (mean: 0.429 nT). The overall correlation coefficient between the observed and model radial field components sampled at 0.5° resolution along the 95 orbit tracks within the mapped area was $R = 0.938$ (> 5900 data points).

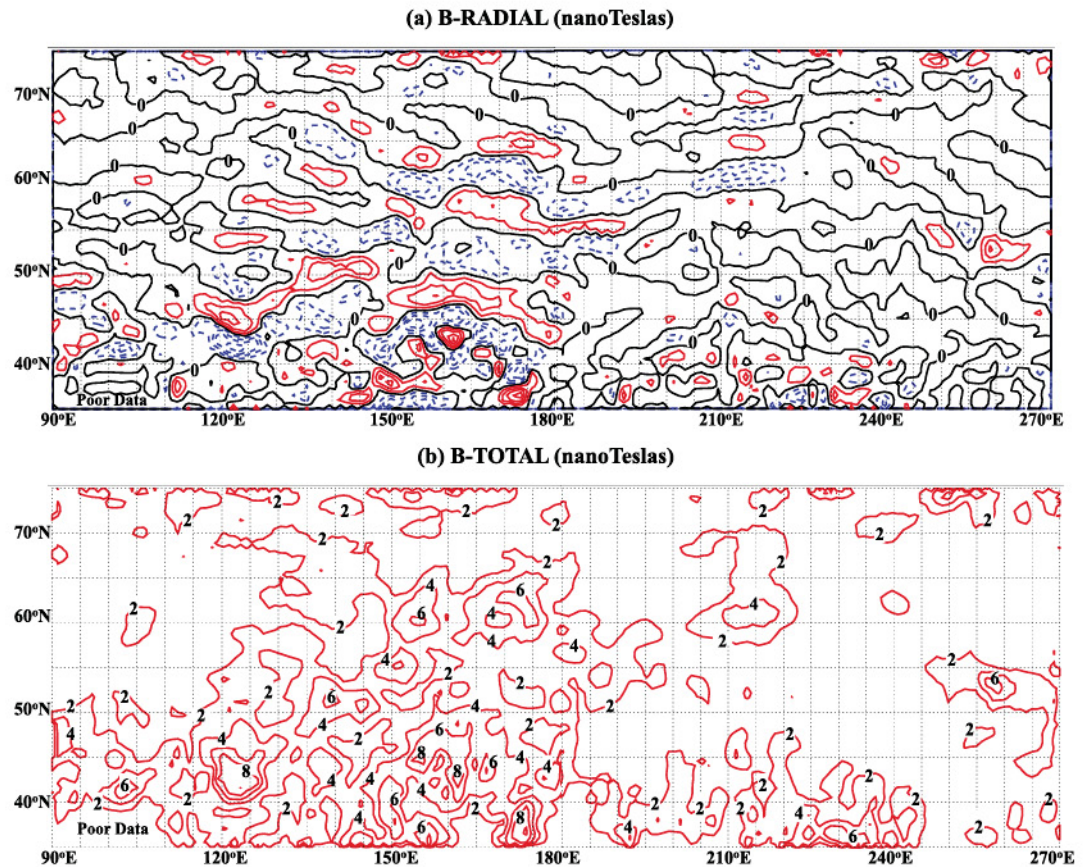


Figure 2. Equivalent Source Dipole modeling results: (a) radial magnetic field intensity at 40 km altitude calculated from the ESD solution; and (b) magnetic field magnitude at 40 km. The contour interval and color scheme for the radial field map are the same as in Figure 3.

3. Results

Figure 2a shows the final model crustal radial field component at an altitude of 40 km, calculated using the model source dipole moments. A constant mapping altitude of 40 km is chosen because it is within the range of measurement altitudes and is comparable to the orbit track separation (about 50 km) at northern midlatitudes. Mapping at much lower altitudes than 40 km, while desirable, can lead to increased errors because the map is effectively undersampled by the wide orbit track separation. Figure 2b shows the field magnitude ("B-Total").

Comparing Figure 2a with Figure 1c, a number of differences are apparent. First, most of the strongest anomalies are now between about 120°E and 180°E, especially near the southern boundary between about 140°E and 180°E. A second group of moderately strong anomalies is also found near the southern boundary between about 210°E and 250°E. As discussed further below, the first area is near and within Caloris while the second group lies near and within Sobkou Planitia and an associated older impact basin. Although a group of strong anomalies is centered near 255°E, 55°N in Figure 1c, after adjustment to a constant altitude, this group is less prominent in Figure 2a but still has a field magnitude maximum of 6 nT in Figure 2b. Finally, the anomalies near 215°E, 65°N (over Suisei Planitia) are less prominent in Figure 2a than in Figure 1c, as expected from the increased altitude. The field magnitude maximum for this anomaly group is only slightly more than 4 nT at 40 km altitude.

4. Comparisons With Surface Geology/Topography

Figure 3a is a superposition of the radial field component map of Figure 2a onto an enhanced color mosaic (B. Denevi, private communication, 2016) derived from the MDIS 3-color basemap [Murchie *et al.*, 2015; Robinson *et al.*, 2008; Chabot *et al.*, 2016]. A superposition of the magnetic field magnitude map of Figure 2b

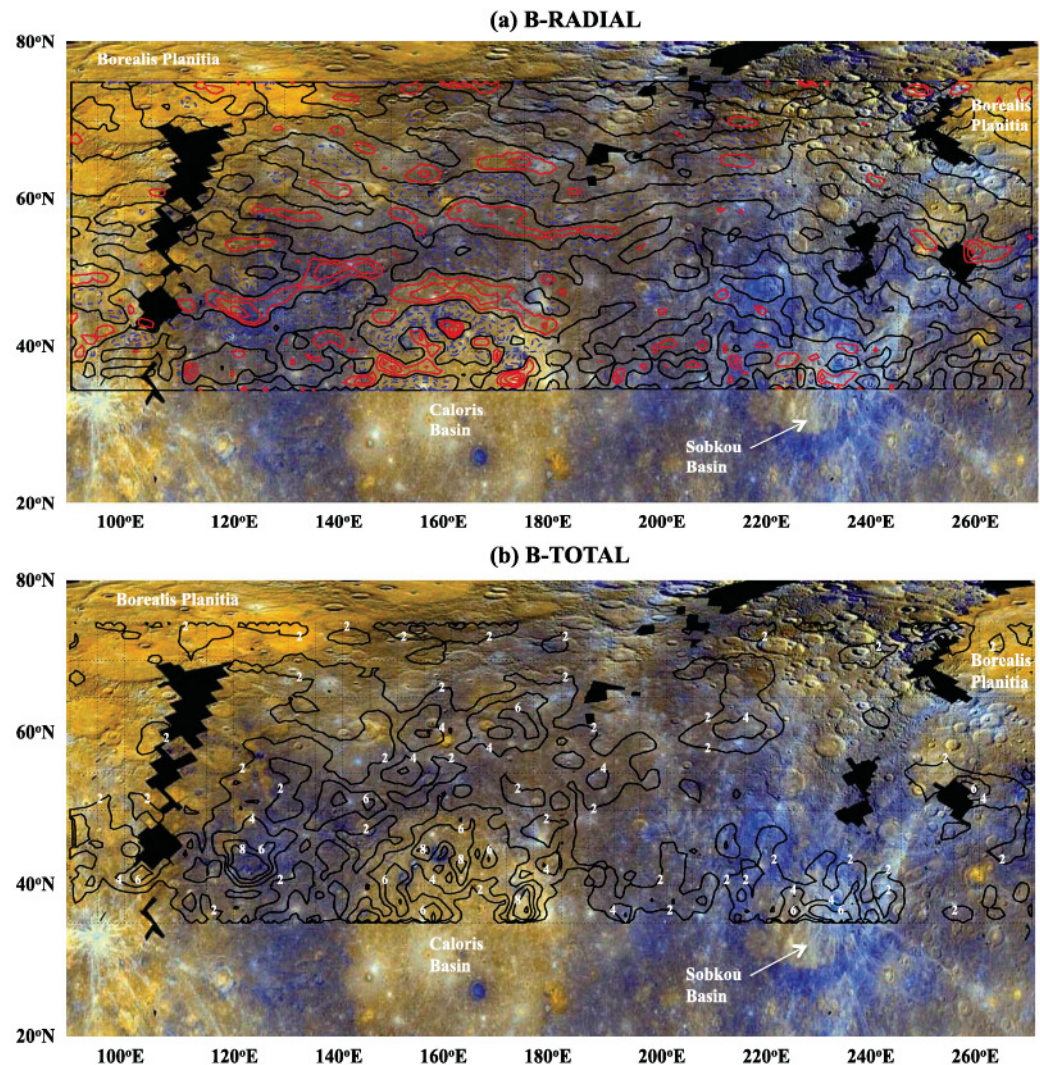


Figure 3. Superposition of the radial field component (a) and field magnitude (b) at 40 km altitude from Figures 2a and 2b onto a MESSENGER enhanced color mosaic (see the text). The contour interval and color scheme for Figure 3a are the same as in Figure 1c.

onto the same color mosaic is shown in Figure 3b. On the mosaic, the reddish-brown areas represent high-reflectance plains (HRP), which are believed to be volcanic in origin and are especially present in the northern lowlands and within Caloris [Murchie et al., 2015]. The darker areas represent low-reflectance material (LRM), which may consist mainly of impact-mixed differentiated crust, including impact basin ejecta. Bluish areas indicate high ratios of reflectance at 430 nm relative to 1000 nm.

Figure 4 shows similar superpositions onto a MESSENGER Laser Altimeter (MLA) elevation map (G. Neumann, private communication, 2016). Also identified in Figure 4a are major geologic features, including several smooth plains (planitias). The unnamed smooth plain with relatively strong radial field anomalies discussed in H15 extends north-northeastward from Caloris.

The most striking anomalies in Figures 3 and 4 are those within Caloris itself. While less than 40% of the basin interior could be mapped from the MESSENGER data, strong positive and negative radial anomalies are prominent within the basin. Plots of the filtered radial field measurements along individual orbit tracks (Figure S3) confirm that the individual radial anomalies mapped within Caloris in Figures 3a and 4a (including that near 173°E, 36°N) are of crustal origin. Along the northern rim of the basin, positive and negative anomalies approximately follow the curvature of the rim (see Figure 5a for a higher-resolution view). Within the northern part of the basin interior, a series of positive (red) radial anomalies are distributed in a semicircular pattern that is

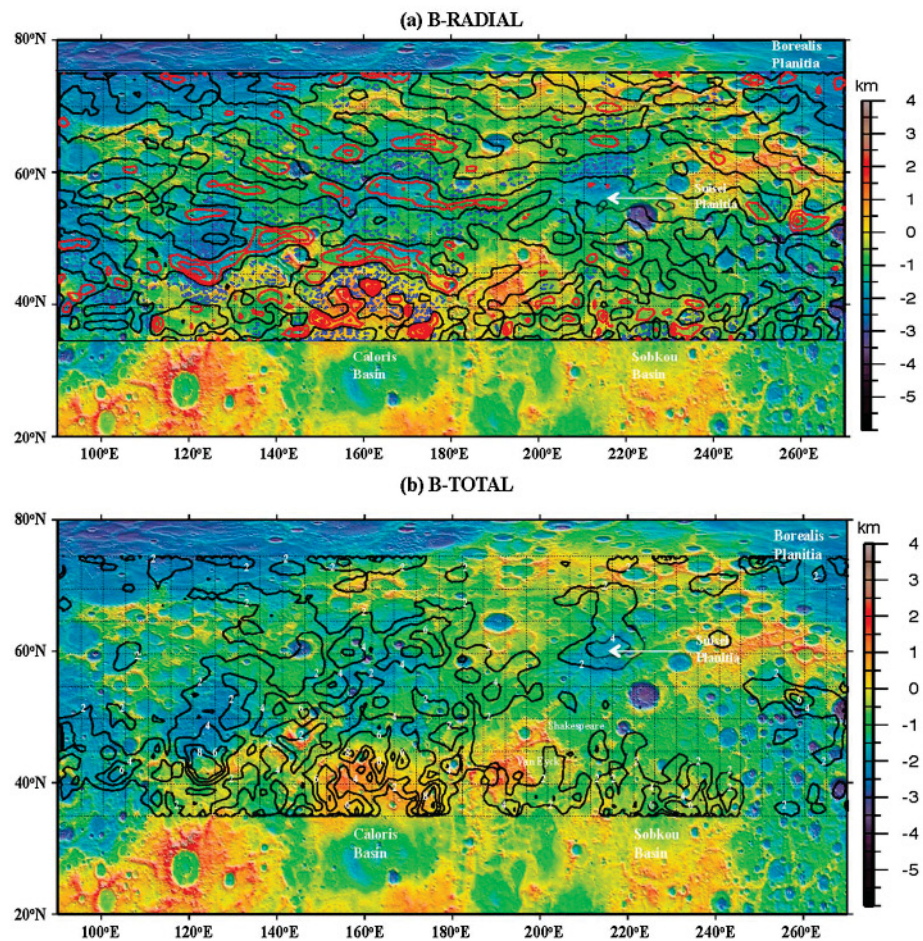


Figure 4. As in Figure 3 but superposed onto a MESSENGER Laser Altimeter elevation map provided by G. Neumann (see the text).

approximately concentric with the basin rim. Anomalies become relatively weak as the center of the basin is approached ($\sim 160^\circ\text{E}$, 35°N). Figure 6a superposes the field magnitude (from Figure 2b) onto a high-resolution image of Caloris. Field amplitudes at 40 km altitude within Caloris are as large as 8 nT along the semicircular arc but decrease to less than 2 nT near the basin center.

A second smaller group of anomalies in Figure 3 is concentrated near and within Sobkou Planitia, which overlies and embays an older impact basin rim [Guest and Greeley, 1983]. See Figures 5b and 6b for higher-resolution views. Anomalies reach amplitudes of 6 nT over the planitia and within the basin rim near 230°E , 36°N (Figure 6b). As shown in Figure S4, the radial anomalies within and near Sobkou Planitia are verified to be crustal in origin by their repetition on successive orbits during two different sets of measurements in February and April of 2015. Anomalies within Sobkou Planitia and its associated older basin are not clearly distributed in patterns that are concentric with the basin rim as they are in Caloris.

As also seen in Figures 3 and 4, anomalies outside of Caloris and Sobkou Planitia are relatively weak over the northern plains (Borealis Planitia) and stronger in the region around Caloris, especially on the western side. If the volcanically resurfaced interior of Caloris and the probable volcanic plain of Sobkou Planitia are excluded, there is a tendency for weaker fields to occur over the reddish-brown areas (HRP) of Figure 3 while stronger fields occur over the darker areas (LRM). As discussed by Murchie *et al.* [2015], LRM is strongly concentrated in impact crater and basin ejecta.

5. Discussion and Conclusions

The magnetic anomalies concentrated within the interior of the Caloris impact basin and within Sobkou Planitia, and its associated older impact basin imply that the Mercurian core dynamo was active at the times

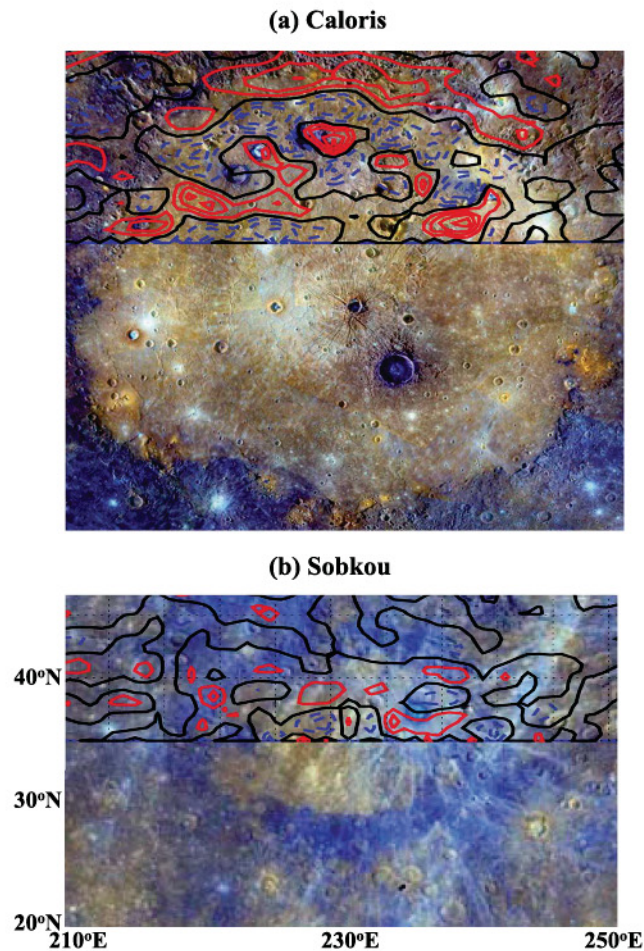


Figure 5. Approximate superposition of the radial field component at 40 km altitude from Figure 2a onto (a) image PIA19216MessengerCaloris.jpg (NASA, Johns Hopkins University APL, Arizona State University, CIW) and (b) a section of the MDIS enhanced color mosaic from Figure 3.

when these impacts occurred. The reasoning for this conclusion is as follows. Numerical simulations show that large crater- or basin-forming impacts on airless silicate bodies would have raised the subsurface within the main rim to a temperature exceeding 1000 K for long time periods following the impact [e.g., *Ivanov, 2005*]. This temperature equals or exceeds the Curie temperature for any likely magnetic remanence carrier (e.g., metallic iron). Any preexisting magnetization or shock-remanent magnetization acquired at the time of impact within these basins would therefore have been thermally erased. It is unlikely that later volcanic intrusions or lava fill could be the anomaly sources because of (a) the weakness of anomalies over volcanic plains elsewhere on Mercury (e.g., Borealis Planitia) and (b) the symmetry of the anomalies about the Caloris basin center. The arrangement of the Caloris anomalies in a semicircular pattern that is roughly concentric with the basin rim is similar to that observed for lunar basins such as Crisium [e.g., *Hood, 2011*]. Such a pattern suggests sources in the form of impact-produced melt rocks or at least sources that formed as a consequence of the impact beneath the visible surface. Such sources would have cooled over long time periods (up to 1 Myr), requiring a long-lived, steady magnetizing field, i.e., an early core dynamo. An early strong solar wind field, for example, would have changed its orientation relative to Mercury continuously during the cooling period, inhibiting any coherent magnetization.

The high-reflectance volcanic lava plains (HRP) inside Caloris and Sobkou apparently did not produce a thermal pulse sufficient to demagnetize the subsurface magnetization acquired during the post-impact period. This is consistent with lunar observations of strong anomalies [e.g., *Reiner Gamma; Hood et al., 1979*] whose sources were later covered by mare basalt with little apparent effect on anomaly amplitude. Thermal diffusion calculations show that relatively thin basaltic lava flows cool efficiently by radiation and do not heat

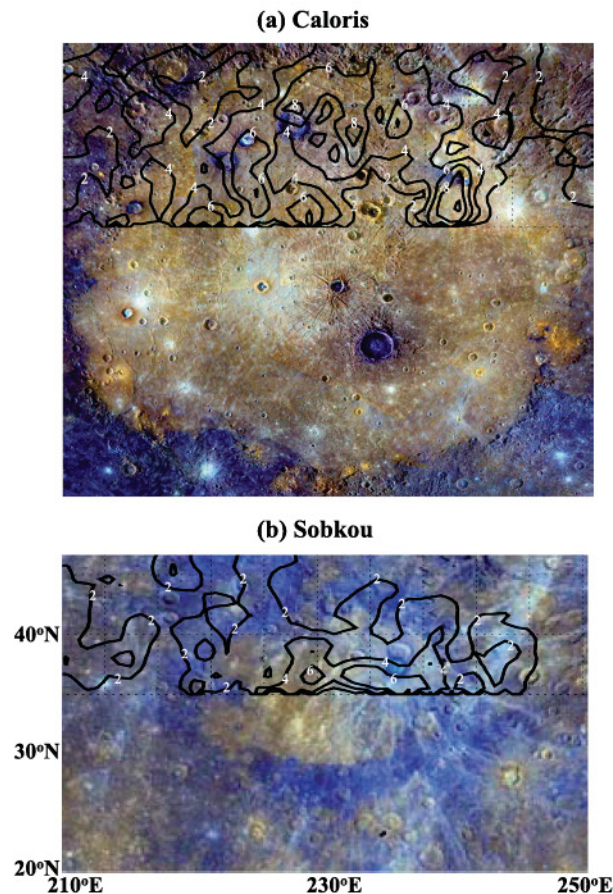


Figure 6. As in Figure 5 but for the magnetic field magnitude from Figure 2b.

subsurface materials to temperatures sufficient to thermally demagnetize plausible anomaly sources at depth [see, e.g., *Rumpf et al.*, 2013]. In contrast to Caloris, the lunar Imbrium and Orientale basins show no internal anomalies even though a core dynamo apparently existed when they formed [e.g., *Shea et al.*, 2012; *Suavet et al.*, 2013]. This may imply that the latter impacts did not produce impact melt containing sufficient magnetic carriers to produce detectable anomalies or that most impact melt was not retained in the basin interior due to the weak lunar gravity field.

Although no absolute ages are available for Mercury's basins, comparisons with the known age of the lunar Imbrium basin together with estimates based on crater size-frequency distributions suggest an age for Caloris of roughly 3.9 Gyr [e.g., *Chapman et al.*, 2015]. The Sobkou rim lies stratigraphically beneath the intercrater plains on Mercury [*Guest and Greeley*, 1983] and so must be considerably older than Caloris, ~ 4.0 Gyr or older. *Marchi et al.* [2013] argue that there is probably nothing visible on Mercury older than 4.1 Gyr. Thus, these results imply that Mercury's core dynamo began to operate at least as early as ~ 4.0 Gyr ago.

A remaining issue is the identities of orbital magnetic anomaly sources outside of the basins. As discussed in H15, the observation that anomalies tend to occur over smooth plains circumferential to Caloris could be consistent with lunar evidence that smooth plains such as the Cayley Formation are sources of many lunar magnetic anomalies [*Strangway et al.*, 1973b; *Halekas et al.*, 2001; *Hood et al.*, 2013]. At least some of the smooth plains around Caloris may have an impact-related origin [*Denevi et al.*, 2013] and could therefore be orbital anomaly sources.

The lunar Cayley Formation is interpreted as impact basin ejecta [*Eggleton and Schaber*, 1972], so the hypothesis that such materials on airless silicate bodies in the solar system are sources of orbital anomalies can be referred to as the "ejecta deposit model." On the Moon, ejecta materials are known to be enriched in microscopic metallic iron remanence carriers, due partly to reduction of preexisting iron silicates by impact-generated heat and shock and partly to the addition of meteoritic iron [*Strangway et al.*, 1973a;

Fuller and Cisowski, 1987; Rochette et al., 2010]. The possible importance of meteoritic iron has led to a variant of the ejecta deposit model in which the sources of the strongest lunar anomalies are proposed to consist of ejecta from an iron-rich impactor that formed the South Pole-Aitken basin [Wieczorek et al., 2012]. On the other hand, most of the same anomalies have been proposed to be a consequence of convergence and deposition of ejecta in enhanced magnetic fields near the antipodes of young large impact basins [Hood and Artemieva, 2008; see also Lin et al., 1988; Mitchell et al., 2008].

As shown in Figure 3, the strongest anomalies around Caloris occur mainly over low-reflectance material. LRM is strongly concentrated in impact crater and basin ejecta [Murchie et al., 2015]. This observation is therefore qualitatively consistent with the ejecta deposit model for the origin of anomaly sources. It is unlikely that the low reflectance of the surface around Caloris is due to the presence of increased amounts of surficial microscopic metallic iron remanence carriers because MESSENGER X-ray spectrometer data, which are sensitive to the uppermost $\sim 100\ \mu\text{m}$, show little or no correlation between reflectance and iron abundance [Weider et al., 2014, 2015]. However, the LRM may be enriched in remanence carriers (e.g., microscopic metallic iron) beneath the visible surface. The darkening agent of LRM probably consists primarily of carbon (graphite) enriched in a primary flotation crust and mixed by impacts [Murchie et al., 2015; Peplowski et al., 2016]. Therefore, if impact-produced materials (ejecta and melt rocks) were enriched in their interiors in both carbon and magnetic carriers, then a correlation between LRM and magnetic anomalies would be expected. Unlike the Moon, there is apparently little if any iron silicate minerals in the Mercurian crust [e.g., Murchie et al., 2015]. If so, then the provenance of the hypothesized iron in Caloris ejecta may be mainly meteoritic, perhaps associated with an iron-rich impactor.

The concentration of magnetic anomalies near impact basins on Mercury differs from the lunar case where anomalies are more widely distributed. Lunar anomalies are not especially strong in the near vicinity of the Imbrium basin, for example [e.g., Hood et al., 1979, 2001; Halekas et al., 2001]. A possible explanation is that the radial extent of both ejecta deposits and secondary crater impacts is smaller for Mercurian basins as compared to lunar basins due to the stronger surface gravity field (2.2 times that of the Moon) [Gault et al., 1975]. Magnetic anomalies around Caloris extend outward to distances comparable to the basin diameter, especially on the western and northern sides (Figures 3 and 4). Since continuous ejecta deposits would extend outward by no more than about 25% of the basin diameter [Gault et al., 1975], it follows that if anomaly sources consist of impact-produced material, it is probably in the form of discrete patches of ejecta or of smooth plains material.

Acknowledgments

MESSENGER calibrated magnetometer data are available from the Planetary Plasma Interactions node of the NASA Planetary Data System (ppi.pds.nasa.gov). The background MLA elevation map and MDIS enhanced color mosaic used in the construction of Figures 3–6 were provided by G. Neumann and B. Denevi, respectively. Thanks to B. Denevi, G. Neumann, P. Spudis, and C. Chapman for informal comments and suggestions that improved the paper. J. Gattacceca and an anonymous reviewer provided further useful comments and suggestions. Also, thanks to the entire MESSENGER mission team for obtaining a remarkable data set.

References

- Chabot, N. L., B. Denevi, S. Murchie, C. Hash, C. Ernst, D. Blewett, H. Nair, N. Laslo, and S. Solomon (2016), Mapping Mercury: Global imaging strategy and products from the MESSENGER mission, Abstract 1256 presented at 47th Lunar and Planetary Science Conference, The Woodlands, Tex., 21–25 Mar.
- Chapman, C. R., C. Fassett, S. Marchi, W. Merline, L. Ostrach, and L. Prockter (2015), Basin formation and cratering on Mercury revealed by MESSENGER, Abstract P53A-2098 paper presented at 2015 Fall Meeting, AGU, San Francisco, Calif., 14–18 Dec.
- Denevi, B., et al. (2013), The distribution and origin of smooth plains on Mercury, *J. Geophys. Res. Planets*, *118*, 891–907, doi:10.1002/jgre.20075.
- Eggleton, R. E., and G. G. Schaber (1972), Cayley Formation interpreted as basin ejecta, in *Apollo 16 Preliminary Science Report, Spec. Publ. SP-315*, edited by L. B. Johnson, pp. 29–7–29–16, NASA, Washington, D. C.
- Fuller, M., and S. Cisowski (1987) edited by J. Jacobs, Lunar paleomagnetism, in *Geomagnetism*, vol. 2, pp. 307–456, Academic Press, Orlando, Fla.
- Gault, D. E., J. E. Guest, J. B. Murray, D. Dzurisin, and M. C. Malin (1975), Some comparisons of impact craters on Mercury and the Moon, *J. Geophys. Res.*, *80*, 2444–2460.
- Guest, J. E., and R. Greeley (1983), *Geologic Map of the Shakespeare Quadrangle of Mercury*, U.S. Geol. Surv. Map I-1408, U.S. Geol. Surv., Arlington, VA.
- Halekas, J. S., D. L. Mitchell, R. P. Lin, S. Frey, L. Hood, M. Acuña, and A. B. Binder (2001), Mapping of lunar crustal magnetic fields using Lunar Prospector electron reflectometer data, *J. Geophys. Res. Planets*, *106*, 27,841–27,852.
- Holschneider, M., A. Chambodut, and M. Mandea (2003), From global to regional analysis of the magnetic field on the sphere using wavelet frames, *Phys. Earth Planet. Inter.*, *135*, 107–124.
- Hood, L. L. (2011), Central magnetic anomalies of Nectarian-aged lunar impact basins: Probable evidence for an early core dynamo, *Icarus*, *211*, 1109–1128.
- Hood, L. L. (2015), Initial mapping of Mercury's crustal magnetic field: Relationship to the Caloris impact basin, *Geophys. Res. Lett.*, *42*, 10,565–10,572, doi:10.1002/2015GL066451.
- Hood, L. L., and N. A. Artemieva (2008), Antipodal effects of lunar basin-forming impacts: Initial 3D simulations and comparisons with observations, *Icarus*, *197*, 485–502.
- Hood, L. L., P. J. Coleman Jr., C. T. Russell, and D. E. Wilhelms (1979), Lunar magnetic anomalies detected by the Apollo subsatellite magnetometers, *Phys. Earth Planet. Inter.*, *20*, 291–311.
- Hood, L. L., A. Zakharian, J. Halekas, D. L. Mitchell, R. P. Lin, M. H. Acuña, and A. B. Binder (2001), Initial mapping and interpretation of lunar crustal magnetic anomalies using Lunar Prospector magnetometer data, *J. Geophys. Res.*, *106*, 27,825–27,839.

- Hood, L. L., N. C. Richmond, and P. D. Spudis (2013), Origin of strong lunar magnetic anomalies: Further mapping and examinations of LROC imagery in regions antipodal to young large impact basins, *J. Geophys. Res. Planets*, 118, 1265–1284, doi:10.1002/jgre.20078.
- Ivanov, B. A. (2005), Numerical modeling of the largest terrestrial meteorite craters, *Sol. Syst. Res.*, 39, 381–409, (Translated from *Astronomicheskii Vestnik*, 39, 426–456).
- Johnson, C. L., et al. (2015), Low-altitude magnetic field measurements by MESSENGER reveal Mercury's ancient crustal field, *Science*, 348, 892–895.
- Langlais, B., M. E. Purucker, and M. Manda (2004), Crustal magnetic field of Mars, *J. Geophys. Res.*, 109, E02008, doi:10.1029/2003JE002048.
- Lin, R. P., K. A. Anderson, and L. L. Hood (1988), Lunar surface magnetic field concentrations antipodal to young large impact basins, *Icarus*, 74, 529–541.
- Marchi, S., C. R. Chapman, C. I. Fassett, J. W. Head, W. F. Bottke, and R. G. Strom (2013), Global resurfacing of Mercury 4.0–4.1 billion years ago by heavy bombardment and volcanism, *Nature*, 499, 59–61.
- Mitchell, D. L., J. S. Halekas, R. P. Lin, S. Frey, L. L. Hood, M. H. Acuña, and A. Binder (2008), Global mapping of lunar crustal magnetic fields by Lunar Prospector, *Icarus*, 194, 401–409.
- Murchie, S. L., et al. (2015), Orbital multispectral mapping of Mercury with the MESSENGER Mercury Dual Imaging System: Evidence for the origins of plains units and low-reflectance material, *Icarus*, 254, 287–305.
- Peplowski, P. N., R. L. Klima, D. J. Lawrence, C. M. Ernst, B. W. Denevi, E. A. Frank, J. O. Goldsten, S. L. Murchie, L. R. Nittler, and S. C. Solomon (2016), Remote sensing evidence for an ancient carbon-bearing crust on Mercury, *Nature Geosci.*, 9, 273–276, doi:10.1038/ngeo2669.
- Purucker, M., D. Ravat, H. Frey, C. Voorhies, T. Sabaka, and M. Acuña (2000), An altitude-normalized magnetic map of Mars and its interpretation, *Geophys. Res. Lett.*, 27, 2449–2452.
- Robinson, M. S., et al. (2008), Reflectance and color variations on Mercury: Regolith processes and compositional heterogeneity, *Science*, 321, 66–69.
- Rochette, P., J. Gattacceca, A. V. Ivanov, M. A. Nazarov, and N. S. Bezaeva (2010), Magnetic properties of lunar materials: Meteorites, Luna and Apollo returned samples, *Earth Planet. Sci. Lett.*, 292, 383–391.
- Rumpf, M. E., S. A. Fagents, I. A. Crawford, and K. H. Joy (2013), Numerical modeling of lava-regolith heat transfer on the Moon and implications for the preservation of implanted volatiles, *J. Geophys. Res. Planets*, 118, 382–397, doi:10.1029/2012JE004131.
- Shea, E. K., B. P. Weiss, W. S. Cassata, D. L. Shuster, S. M. Tikoo, J. Gattacceca, T. L. Grove, and M. D. Fuller (2012), A long-lived lunar core dynamo, *Science*, 335, 453–456.
- Strangway, D. W., W. Gose, G. Pearce, and R. McConnell (1973a), Magnetism and the history of the Moon, in *Magnetism and Magnetic Materials—1972*, edited by C. Graham Jr. and J. Rhyne, pp. 1178–1187, Am. Inst. of Phys., New York.
- Strangway, D. W., H. Sharpe, W. Gose, and G. Pearce (1973b), Lunar magnetic anomalies and the Cayley Formation, *Nature*, 246, 112–114.
- Suavet, C., B. P. Weiss, W. Cassata, D. Shuster, J. Gattacceca, L. Chan, I. Garrick-Bethell, J. W. Head, T. Grove, and M. D. Fuller (2013), Persistence and origin of the lunar core dynamo, *Proc. Natl. Acad. Sci. U.S.A.*, 110, 8453–8458.
- Thébault, E., J. J. Schott, and M. Manda (2006), Revised spherical cap harmonic analysis (R-SCHA): Validation and properties, *J. Geophys. Res.*, 111, B01102, doi:10.1029/2005JB003836.
- von Frese, R. R. B., W. J. Hinze, and L. W. Braille (1981), Spherical Earth gravity and magnetic anomaly analysis by equivalent point source inversion, *Earth Planet. Sci. Lett.*, 53, 69–83.
- Weider, S. Z., L. R. Nittler, R. D. Starr, T. J. McCoy, and S. C. Solomon (2014), Variations in the abundance of iron on Mercury's surface from MESSENGER X-Ray spectrometer observations, *Icarus*, 235, 170–186.
- Weider, S. Z., et al. (2015), Evidence for geochemical terranes on Mercury: Global mapping of major elements with MESSENGER's X-Ray Spectrometer, *Earth Planet. Sci. Lett.*, 416, 109–120.
- Wieczorek, M. A., B. P. Weiss, and S. T. Stewart (2012), An impactor origin for lunar magnetic anomalies, *Science*, 335, 1212–1215.